

Chirality induced spin selectivity in chiral crystals

Qun Yang^{1,2,†}, Yongkang Li^{2,†}, Claudia Felser¹, and Binghai Yan^{2,*}

¹Max Planck Institute for Chemical Physics of Solids, 01187 Dresden, Germany.

²Department of Condensed Matter Physics, Weizmann Institute of Science, Rehovot 7610001, Israel

[†]These authors contributed equally

*binghai.yan@weizmann.ac.il

ABSTRACT

Chirality is a fundamental property of great importance in physics, chemistry, and biology. Recently, an exotic phenomenon known as chirality-induced spin selectivity (CISS), in which electrons with a particular spin can pass through chiral molecules, has shown promising application potential in spintronic devices, spin control chemistry, and enantiomer separation, among others. However, current CISS studies focus mainly on chiral organic molecules with poor electronic conductivity and inherent complexities, such as the controversial role of SOC at the molecule-metal interface. In contrast, chiral inorganic materials with excellent electrical conductivity, intrinsic SOC, homochiral crystal structure, and rich electronic properties open up new possibilities for advancing CISS studies. In this work, we demonstrate that electrons exhibit both spin and orbital polarization as they pass through chiral crystals. Both polarizations increase with material thickness until approach bulk properties. The spin polarization correlates with the SOC strength, while the orbital polarization is SOC insensitive. Furthermore, our results reveal a substantial spin polarization ratio in Te and significant electrical magneto-chiral anisotropy in RhSi. Though the latter is usually employed to probe the former, the results show a clear difference between these two quantities. Our work reveals the interplay of chirality, electron spin, and orbital in chiral crystals, paving the way for the development of chiral inorganic materials for CISS applications.

INTRODUCTION

Chirality, which refers to a unique spatial asymmetry including the absence of a mirror plane and an inversion center, is a fundamental concept with far-reaching implications in the realms of chemistry, biology, and physics¹. Recently, structural chirality was found to induce electronic chirality, manifesting as orbital-momentum locking encoded in the wave function of chiral molecules or solids^{2,3}. Furthermore, the combination of structural chirality with topological band structures leads to chiral multi-fold fermion crossings characterized by parallel spin-momentum locking (**Fig. 1a**)⁴⁻⁷. These findings reveal a deep connection between chirality in the real and reciprocal space of quantum materials, providing an ideal playground for the study of exotic physical phenomena. One of the exotic phenomena known as chirality-induced spin selectivity (CISS), in which electrons with particular spin can pass through chiral materials (**Fig. 1b**), generates remarkable spin polarization without the need for magnetic fields or magnetism^{8,9}. This particular feature of the CISS effect is not only of fundamental importance for understanding the underlying mechanism of electron dynamics in chiral objects but also offers practical promise for various applications, including the field of spintronic devices^{8,10,11}, spin control chemistry^{9,12-14} and enantiomer separation^{15,16}.

To date, most CISS studies have been carried out on chiral molecules¹⁷⁻¹⁹, self-assembled chiral molecular films^{20,21}, metal-organic frameworks²², chiral organic-inorganic hybrid perovskites^{23,24} and chiral molecular intercalation superlattices^{25,26}. In these systems, organic chiral molecules bring chirality but also complexity such as the debating role of spin-orbit coupling (SOC) at the molecule-metal interface^{2,27}. In contrast, inorganic crystals with homochiral crystal structures and rich electronic structures open up a range of new possibilities for the CISS effect. Recently, it has been experimentally observed that chiral crystals of Te^{28,29}, CrNb₃S₆³⁰ and TMSi₂ (TM = Nb, Ta)³¹ exhibit a spin-polarized state when

subjected to charge current injection. Theoretically, the physical origin of the observed phenomenon remains elusive. Existing theories have endeavored to provide an explanation by linking it to the Edelstein effect that emerges from the radial spin texture and spin imbalance²⁸ However, the Edelstein effect refers to uniform magnetization inside the crystal induced by a non-spin-polarized current^{3,32,33} and is not fully equivalent to the spin-polarized current generated by electrons transporting through the chiral material.

In this work, we perform first-principles quantum transport calculations on chiral crystals and evaluate the spin polarization of current induced by the chirality. We find that electrons transmitted through these chiral crystals exhibit both spin and orbital polarization. Both polarizations align along the transport direction and increase with the propagating distance before saturating when the system approaches bulk properties, consistent with the length-enhanced spin polarization observed in chiral molecules. Comparing various compounds with the same structural and electronic properties, we reveal that induced spin polarization is proportional to the SOC magnitude while orbital polarization is insensitive to SOC. Furthermore, we find a spin polarization ratio of up to 40% in Te, originating from the large spin splitting at the valence band edge. The pronounced spin polarization leads to a substantial electric magneto-chiral anisotropy (EMCA) when probed by magnetic electrodes. We demonstrate that RhSi exhibits a magneto-current ratio (0.22%) upon flipping the electrode magnetization, which is larger than the relative change of magneto-resistance in recent experimental observations of the EMCA effect in chiral crystals and microhelices. The distinction between the spin polarization and magneto-current ratio is emphasized in our calculation. Our results pave the way to understanding the CISS effect in inorganic crystals and explore emerging chirality-driven phenomena.

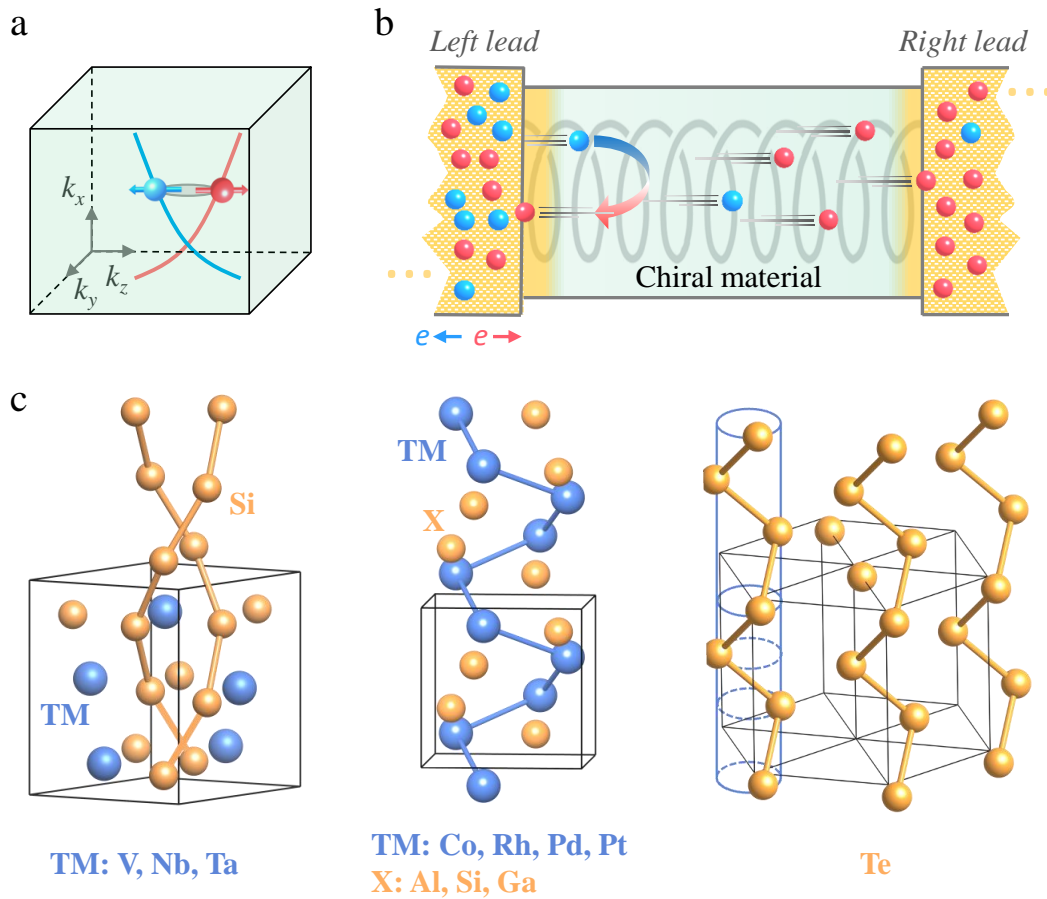


Figure 1. Schematic illustration of the two-terminal device setup for the chirality-induced spin selectivity (CISS) effect in chiral crystal and crystal structures of representative chiral materials. a. Illustration of the electronic chirality of spin-momentum locking on the band structure of chiral materials. **b.** Geometry of the transport model. The chiral crystal is placed in the central region, which is periodically repeated in the transverse direction but finite in the transport direction. The chiral crystal seamlessly connects with two leads. The electrons with opposite spins (red and blue spheres) moving through the chiral central region become spin-polarized. The chiral crystal acts as the spin polarizer so that the transmitted and reflected electrons exhibit the same type of spin polarization. **c.** Chiral crystal structures of the transition metal disilicide TMSi₂ (TM = V, Nb, Ta), FeSi-type B20 materials TMX (TM = Co, Rh, Pd, Pt; X = Al, Si, Ga), and trigonal tellurium (Te). Their chirality can be distinguished by the helical chains formed by Si, TM, and Te atoms, respectively

RESULTS AND DISCUSSION

Among the 230 space groups (SGs), 65 are designated as Sohncke SGs for chiral structures. Within these, 22 are enantiomeric, forming 11 enantiomorphous pairs, such as $P6_1$ and $P6_5$. Additionally, there are 43 non-enantiomeric SGs, each containing two enantiomers that share identical spatial symmetry but inverted atomic positions, such as $P6_3$ and $P2_13$. In our research, we consider three catalogs of representative chiral crystals, including 1) Intermetallic transition metal disilicides, specifically $TMSi_2$ (TM=V, Nb, and Ta). These crystals adopt C40 structures and belong to the enantiomeric SG $P6_222$ (No. 180) or SG $P6_422$ (No. 181). 2) Topological multifold semimetals, in particular TMX compounds (TM = Co, Rh, Pd, Pt, and X = Al, Si, Ga). These materials crystallize in B20 (FeSi type) structures and belong to the non-enantiomeric SG $P2_13$ (No. 198). The topological trivial insulator RhBiS is also included. 3) Semiconductor γ -Se and Te, characterized by a trigonal crystal system and belonging to the enantiomeric SG $P3_121$ (No. 152) or $P3_221$ (No. 154). **Fig. 1c** shows the crystal structures of these chiral materials in one of their enantiomeric forms, the chirality can be visualized by the helical winding patterns of the atoms.

To investigate the dynamic CISS process in these chiral crystals, we constructed a two-terminal CISS device for quantum transport calculations, as depicted schematically in **Fig. 2a**. The chiral crystal with finite thickness along the [001] transport direction is positioned on the central region, which is connected with two semi-infinite leads on its left and right sides. In both leads, we employed the wide-band limit (WBL)^{34,35} approximation, assuming a constant density of states (DOS) that disregards the detailed structure of the DOS in the leads. This approximation is commonly used to describe transport in nanoscale devices, which substantially simplifies computations. Within the WBL framework, the spin and orbital polarization can be accurately defined within the leads. The inherent SOC within the chiral crystals facilitates preferential spin/orbital polarization of the transmitted electrons, depending on the current

direction and handedness of the chiral crystal. Employing this model, we calculated the conductance (G) using the Landauer-Büttiker formalism³⁶, which involves the transmission function from left (L) to the right (R) lead,

$$G_{\text{RL}} = \frac{e^2}{h} \sum_{n \in \text{R}, m \in \text{L}} |S_{nm}|^2 \quad (1)$$

where S_{nm} is the scattering matrix element from the m th eigenstate in L lead to the n th eigenstate in R lead.

With the spin and orbital conserved leads, the spin- and orbital-polarized conductance can be obtained as

$$G_{\text{RL}}^{S_z} = \frac{e^2}{h} \sum_{n \in \text{R}, m \in \text{L}} S_{z,n} |S_{nm}|^2 \quad (2)$$

$$G_{\text{RL}}^{L_z} = \frac{e^2}{h} \sum_{n \in \text{R}, m \in \text{L}} S_{L,n} |S_{nm}|^2 \quad (3)$$

$G_{\text{RL}}^{S_z(L_z)}$ is the conductance from L lead to the $S_z(L_z)$ channel of R lead. $S_{z,n}(L_{z,n})$ is the z -component of spin (orbital) angular momentum carried by the transmitted electron in mode n of the R lead. The corresponding spin- and orbital-polarization ratio can be calculated by $P_{S_z} = \frac{G_{S_z}}{G} \times 100\%$ and $P_{L_z} = \frac{G_{L_z}}{G} \times 100\%$, respectively. In the following discussion, we use $P_{S_z(L_z)}$, $G_{S_z(L_z)}$, and G for $P_{\text{RL}}^{S_z(L_z)}$, $G_{\text{RL}}^{S_z(L_z)}$, and G_{RL} , respectively, if it is not noted specifically.

Experimental observations of the CISS effect on chiral molecules reveal a notable correlation between the induced spin polarization and the molecular length^{17,37}. To explore this phenomenon in chiral crystal, we initially examined the dependence of the P_{S_z} and P_{L_z} on the thickness of chiral material TaSi₂ in the central scattering region, quantified by the number of unit cells (N) in the transport direction (the [001] direction). As shown in **Fig. 2b-c**, the results confirm the coexistence of P_{S_z} and P_{L_z} , attributing to the presence of the intrinsic SOC and inversion symmetry breaking within the chiral material. Especially, the P_{S_z} exhibits an initial increase followed by a saturation when N reaches ten, indicating a thickness-enhanced spin polarization in chiral crystal with saturation occurring when the system reaches a bulk characteristic. While P_{L_z} exhibits an initial increase until $N=4$, followed by a slight decrease, and then

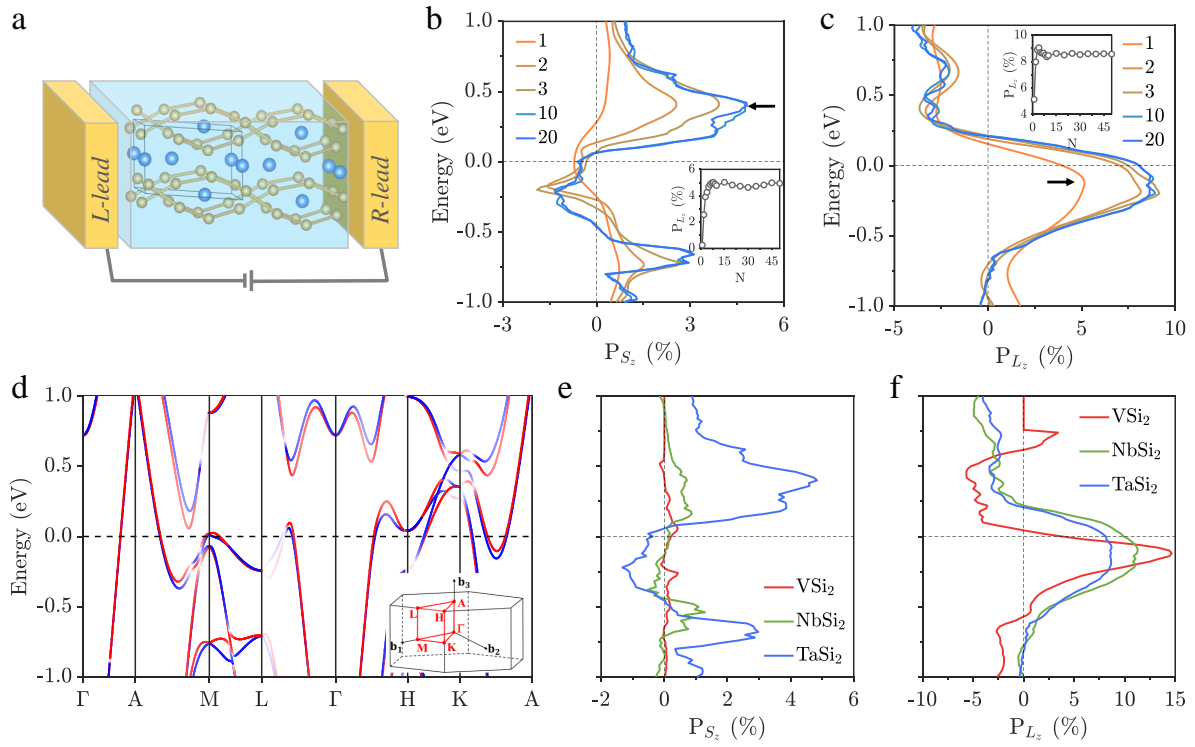


Figure 2. Spin polarization and orbital polarization in the conductance of transition metal disilicide TMSi₂ compounds. **a.** The transport model consists of two leads and the chiral material TaSi₂ with thickness NL along the $[001]$ transport direction in the central region. N and L denote the number of unit cells and the lattice constant along the crystal c -axis. $N=2$ is shown in schematic. **b.** Energy-dependent spin polarization ratio (P_{S_z}) and **c.** orbital polarization ratio (P_{L_z}) of TaSi₂ for $N=1, 2, 3, 10$ and 20 . Peaks of P_{S_z} and P_{L_z} (see inset in **b** and **c**, respectively) increase rapidly with increasing N and approach saturation when N reaches 10 . For all subsequent calculations, N is fixed at 20 to fundamentally explore the intrinsic bulk band structure effect on spin and orbital polarization. **d.** Spin angular momentum (SAM) resolved band structures of TaSi₂ in the Brillouin zone. The color red (blue) represents spin-up (down) states. Energy-dependent **e.** P_{S_z} and **f.** P_{L_z} for VSi₂, NbSi₂, and TaSi₂, respectively. The Fermi energy lies at the charge neutral point.

reaches saturation at around $N=10$. Moreover, we point out that the chiral crystal acts as the spin polarizer³⁸ (orbital polarizer), resulting in the transmitted and reflected electrons exhibiting the same type of spin polarization (orbital polarization), as confirmed by our transmitted/reflected spin (orbital) conductance calculations. Furthermore, P_{S_z} and P_{L_z} reverse its sign for opposite enantiomers A and B: $P_{S_z}^A = -P_{S_z}^B$; $P_{L_z}^A = -P_{L_z}^B$ (**Fig. S1**).

To understand the origin of the chirality-induced spin and orbital polarization in chiral material, the spin angular momentum (SAM)- and orbital angular momentum (OAM)-resolved band structures of TaSi₂ are further analyzed. TaSi₂ in SG P6₂22 possesses threefold screw rotation $\{C_{3z}|0,0,2/3\}$ and twofold rotations $\{C_{2,110}|0,0,2/3\}$ and $\{C_{2z}|0,0,0\}$ as the symmetry generators. These symmetries impose constraints on the SAM and OAM in the momentum space. We found that the z-component of SAM and OAM must vanish along all high symmetry lines in the $k_z = 0$ and $k_z = \pi$ planes. As an illustration, the high-symmetry line Γ -K ($k_x=k_y=k$, $k_z=0$) remains invariant under the $C_{2,110}$ axis, resulting in $L_z(k, k, 0) = 0$. Therefore, the SAM- and OAM-resolved band structures are computed for TaSi₂ along the selected k-paths where $S_z(k)$ and $L_z(k)$ are non-zero. As shown in **Fig. 2d** and **Fig. S2**, the chiral crystalline symmetries and strong SOC in TaSi₂ result in a large spin-splitting of the bands. We found that the spin-split bands carry the opposite SAM but approximately the same OAM. This induces the spin and orbital polarization as electrons move through the chiral crystal and generally a larger magnitude of P_{L_z} than P_{S_z} in the presence of current flow. At the charge neutral point, the calculated P_{S_z} and P_{L_z} in TaSi₂ is -0.57% and 7.95%, respectively.

Fig. 2e and **Fig. 2f** shows the energy-dependent P_{S_z} and P_{L_z} for TaSi₂-family of materials, including TaSi₂, NbSi₂, and VSi₂. We found that the P_{L_z} is insensitive to the SOC strength of different materials, reaching the maximum value of 14.60% at -0.10 eV in VSi₂. In contrast, P_{S_z} shows a clear correlation with the SOC strength in materials. The peaks of P_{S_z} appear at positions with pronounced spin splitting in

the band structure. Especially, within a wide energy range, the P_{S_z} increases as SOC strength increases in V-3d, Nb-4d and Ta-5d³⁹. For instance, the calculated P_{S_z} at peak 0.21 eV are 0.08%, 0.62%, and 3.83% in VSi₂, NbSi₂, and TaSi₂, respectively. The maximum P_{S_z} value of 4.84% is observed at 0.41 eV for TaSi₂. It's noted that the CISS effect has predominantly been explored in chiral organic molecules with P_{S_z} values exceeding 60%^{9,25,26}. By contrast, the magnitude of P_{S_z} in chiral crystals is small. However, considering the excellent electrical conductivity with exceptionally high carrier density in these chiral metals compared with in chiral organic molecules, we expect that the CISS in the chiral crystal is promising for application in spintronic devices, spin-selective chemical reactions, and enantiomer recognition, which remains poorly explored in chiral inorganic crystals^{30,31,40}.

Next, we studied the CISS effect within the family of chiral materials belonging to SG P2₁3. **Fig. 3** illustrates the calculated P_{S_z} and P_{L_z} of various representative topological chiral semimetals within this SG, including the RhSi family (CoSi, RhSi, and RhSn) and PdGa family (PdAl, PdGa, PtAl, and PtGa), based on their elemental similarities. These materials are characterized by multiple band crossings with large Chern numbers in the bulk state and unique Fermi arcs at surfaces^{6,41-43}. The z-component of their SAM- and OAM-resolved band structures are displayed in **Fig. S3** and **Fig. S4**. We found that the P_{S_z} values of the RhSi family of materials do not exhibit a clear trend. The sharp peaks observed at -0.52 eV and -0.58 eV in CoSi, -0.91 eV in RhSi, and -0.71 eV in RhSn primarily arise from the low total conductance at the band edge. Notably, RhBiS is identified as a topological trivial semiconductor⁴⁴ with an indirect band gap of approximately 0.25 eV by our GGA-PBE calculation. The top of its occupied bands is mainly dominated by the Bi-6*p* orbital, leading to significant spin splitting. We found that the spin polarization disappears within the band gap, but it exhibits a relatively large value of about 5% across a wide energy range spanning from -0.6 eV to -0.1 eV, surpassing that of CoSi, RhSi, and RhSn. For the PdGa family of materials, the PtAl and PtGa exhibit evident enhanced P_{S_z} values compared to PdAl and

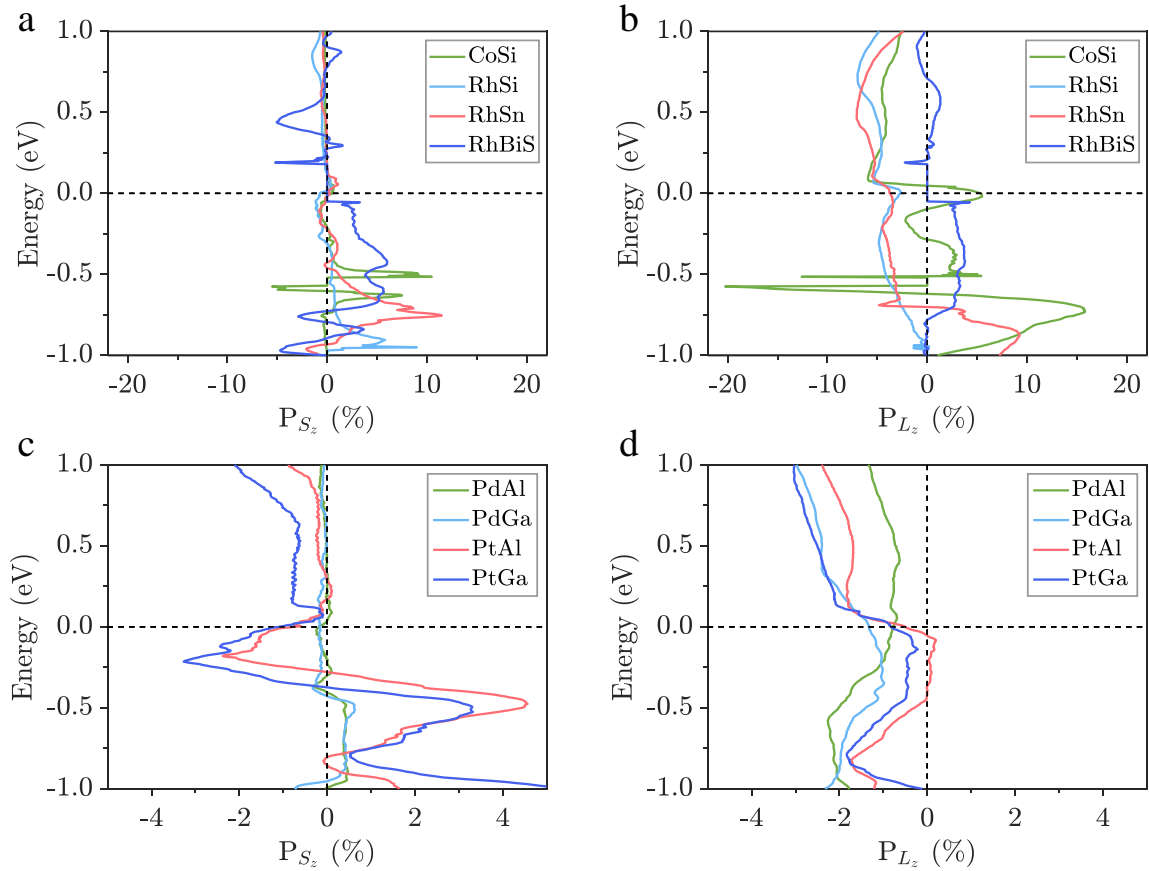


Figure 3. Spin and orbital polarization in the conductance of some representative chiral materials with the SG $P2_13$. The graph displays the values of P_{S_z} and P_{L_z} for topological chiral semimetals within the FeSi-type B20 class, including members from the RhSi family (CoSi, RhSi, and RhSn), as well as the PdGa family of materials (PdAl, PdGa, PtAl, and PtGa). Additionally, the figure includes data for the semiconducting chiral material, RhBiS.

PdGa. At the energy of -0.48 eV, where the peak appears, the calculated P_{S_z} values are 0.40%, 0.59%, and 4.53%, 3.18% for PdAl, PdGa, PtAl and PtGa, respectively. This is probably because Pt atoms have larger atomic numbers and hence stronger SOC effects than Pd atoms. Recent studies reveal that the topological chiral semimetals such as PdGa show promising applications in enantioselective catalytic reactions of chiral molecules^{16,45,46}, which is a signature of the existence of the exotic interplay between the structural chirality of the material and its electron spin or orbital transport properties³. Our results reveal that the presence of the specific spin and orbital polarization carried by the transmitted electrons through PdGa will facilitate the theoretical understanding of the enantioselective chemistry in the material.

Generally, semiconductors or insulators, with their significantly lower carrier density, will show a larger magnitude of spin polarization compared to metals. $\gamma - Se$ is a semiconductor with a large indirect band gap of 1.058 eV by our GGA-PBE calculations, where the valence band maximum (VBM) and conduction band minimum (CBM) are located at the L and H points of the Brillouin Zone (BZ), respectively, as shown in **Fig. 4a**. We found that P_{S_z} is smaller than P_{L_z} in $\gamma - Se$ with the amplitude of a few percent near the Fermi level. Particularly, Te is also a semiconductor, but with a direct band gap of 0.142 eV formed at the H points. The strong spin-orbit interaction in Te causes a substantial separation of 0.126 eV between the two upper branches of the valence band at the H point, significantly impacting its electrical transport properties. We found that the P_{L_z} is greater than P_{S_z} in the conductance band region. However, the trend is reversed in the valence band region with P_{S_z} typically dominating over P_{L_z} (**Fig. 4d**). Strikingly, a sharp peak with a giant P_{S_z} of approximately 40% is observed around the valence band edge. This high P_{S_z} is attributed to the single band occupancy, as the closest band in energy with an opposite SAM is largely separated with the valence band edge (**Fig. 4c**). This situation is ideal for maximizing the P_{S_z} and, consequently, the CISS effect. We point out that the giant P_{S_z} observed in Te is comparable to the value reported in chiral organic molecules and is at least one order of magnitude larger than that obtained in

chiral crystals of transition metal disilicides and topological chiral semimetals.

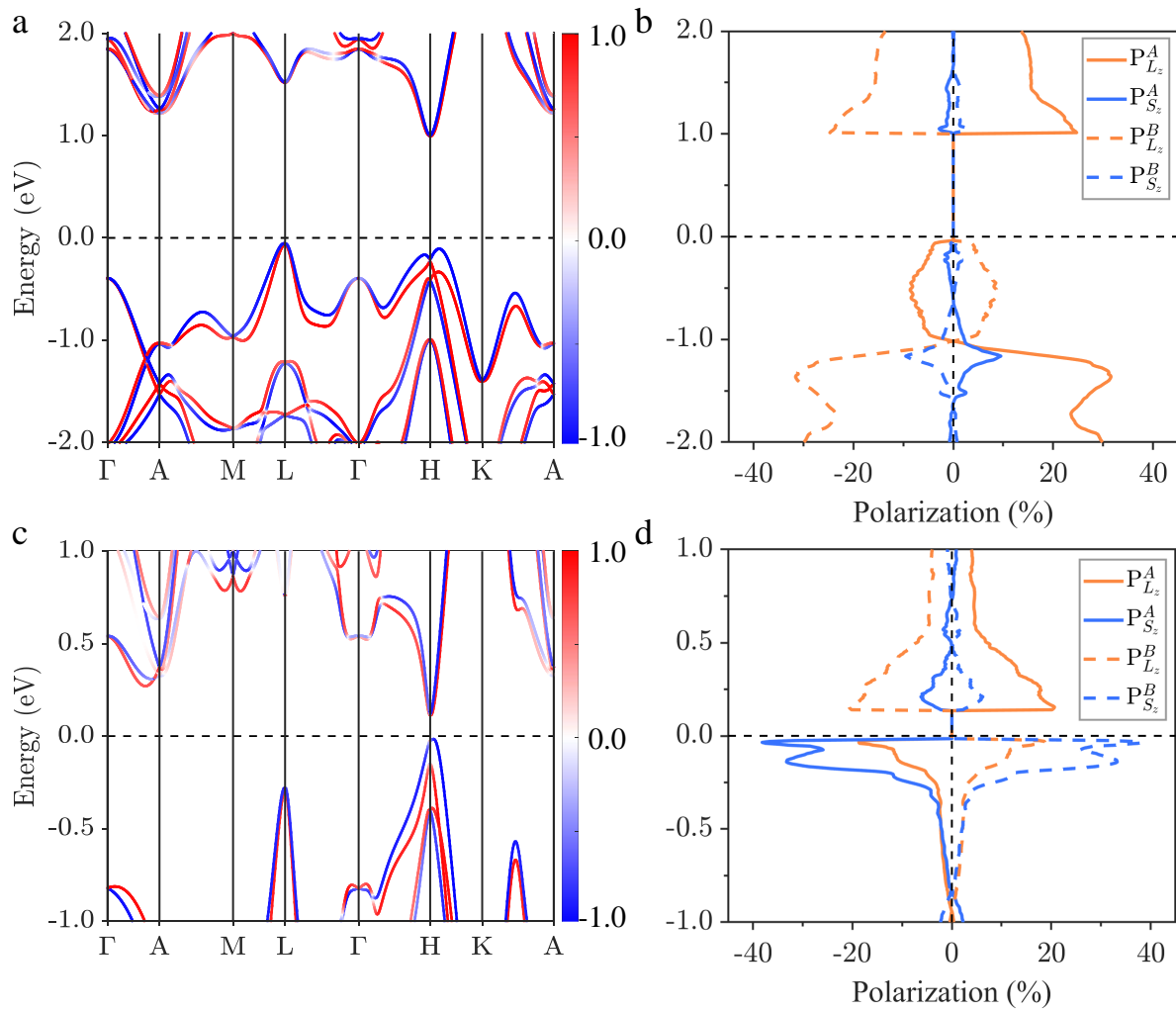


Figure 4. Spin polarization and orbital polarization in the conductance of γ -Se and Te. SAM-resolved band structures of the enantiomer A of **a.** γ -Se and **c.** Te. The color red (blue) represents spin up (down) states. P_{S_z} and P_{L_z} in enantiomer A ($P_{S_z}^A$, $P_{L_z}^A$) and B ($P_{S_z}^B$, $P_{L_z}^B$) of **b.** γ -Se and **d.** Te.

In experiments, CISS is commonly probed through two-terminal magnetoresistance (MR) measurements, with a chiral molecule sandwiched between a ferromagnetic substrate and a nonmagnetic lead^{23,25,47}. The induced spin polarization from chiral molecules leads to resistance changes when flipping the substrate magnetization (M). We highlight that in the context of CISS, the induced spin polarization can also lead to electrical magneto-chiral anisotropy (EMCA) transport⁴⁸, which is usually reported in

chiral solids. It refers to the resistance that depends on the handedness of the conductor and on the relative orientation of electrical current I and magnetic field B . The EMCA resistance is described by the equation $R^\chi = R_0(1 + \alpha B^2 + \beta^\chi B \cdot I)$, where $\beta^\chi = -\beta^{-\chi}$ and $\chi = \pm$ represents the chirality. The B^2 term represents the ordinary magnetoresistance. Notably, the $B \cdot I$ term is specific to chiral conductors, indicating the presence of unidirectional magnetoresistance (UMR): $R^\chi(I, B) \neq R^\chi(I, -B)$. EMCA transport respects the Onsager's reciprocal relation, signifying the presence of time reversal symmetry⁴⁸. By contrast, CISS MR violates this reciprocity, leading to a fundamentally distinct symmetry in the I-V curves and conductance compared to EMCA⁴⁹⁻⁵³. Our recent study reveals a close relationship between EMCA and CISS MR, with EMCA predominantly manifesting in chiral conductors⁵⁴. Experimentally, such EMCA has been demonstrated in many chiral solids, including bismuth helices⁴⁸, carbon nanotubes^{55,56}, bulk organic conductors⁵⁷, tellurium semiconductor^{28,58}, metals with intrinsic magnetic order^{59,60}, and superconductors⁶¹, in which the relative amplitude of UMR was usually several percent or even less, while the CISS MR can be larger than 60% in chiral molecule device^{25,26}.

The distinct CISS effect that is characterized by the P_{S_z} value observed in chiral materials motivate us to explore their EMCA response. We employed the same two-terminal model as in the spin polarization calculation above but introduced a magnetization along the z direction in both leads to mimic the effect of the magnetic field, as depicted in **Fig. 5a**. Inelastic scattering is taken into account by introducing a dephasing parameter $i\eta$ in the central region. This dephasing term breaking the current conservation is necessary to have nonzero magneto-resistance². The resulting I-V curve of RhSi is shown in **Fig. 5c**, where spin polarization in the transmission current leads to the UMR effect, i.e. $I(V, M) \neq I(V, -M)$ in the system. But Onsager's reciprocal relation $I(V, M) = -I(-V, -M)$ still holds showing that UMR is mainly caused by EMCA in the chiral conductors. To characterize this UMR effect, the magneto-current ratio is defined as $P_M = \frac{I(V, M) - I(V, -M)}{I(V, M) + I(V, -M)} \times 100\%$ ⁶². **Fig. 5d** displays the calculated P_M for RhSi. Additional results

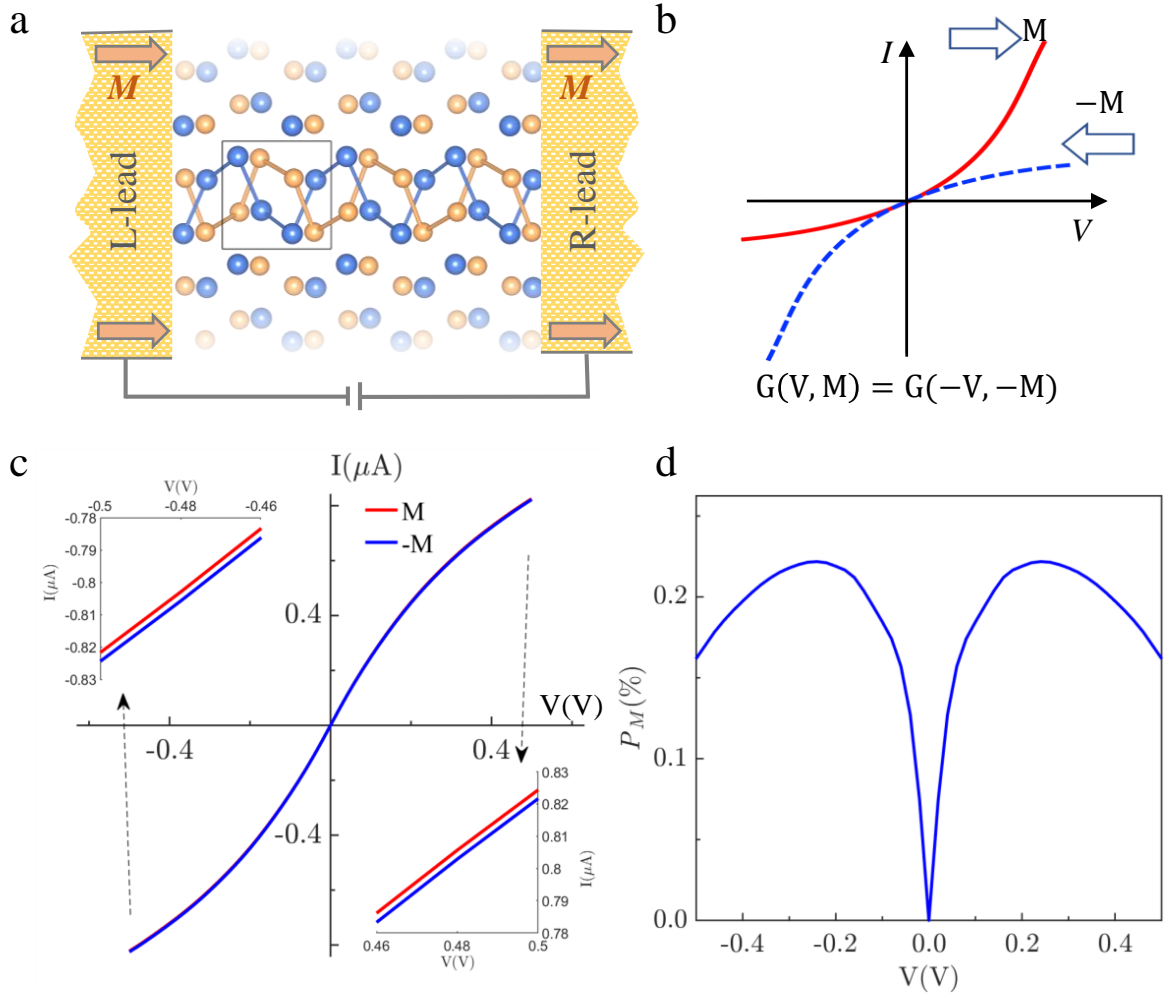


Figure 5. Magneto-current in RhSi. **a.** Schematic representation of the device setup for electrical magneto-chiral anisotropy (EMCA), with a chiral crystal connecting magnetized leads. The conductance and current are high (low) when the electron spin aligns parallel (or anti-parallel) to the electrode magnetization M . **b.** Typical current-voltage (I - V) curves for EMCA. The colors represent the electrode magnetization direction. **c.** The I - V curves of EMCA in RhSi. EMCA respects Onsager's reciprocal relation that the magnitude of current in a two-terminal setup remains invariant when the bias voltage (V) and magnetism (M) are reversed, i.e., $I(V, M) = -I(-V, -M)$ as shown in the inset. **d.** Magneto-current ratio in RhSi. The magneto-current ratio $P_M = \frac{I(V, M) - I(V, -M)}{I(V, M) + I(V, -M)} \times 100\%$ increases with increasing magnitudes of $\Delta\Gamma/\Gamma$ which is a representation of magnetization M .

for other chiral compounds are presented in **Fig. S5**. We found that the P_M increases with the magnitude of the magnetization (M), as denoted by the spin-polarized DOS ratio $\Delta\Gamma/\Gamma$ (see Supplementary Information). Especially, at the maximal M ($\Delta\Gamma/\Gamma=0.5$), P_M first increases with bias and then decreases, exhibiting a peak value $P_M = 0.22\%$ around $V = \pm 200\text{meV}$. Noteworthy, the magnitude of P_M is larger than the observed relative change of magneto-resistance due to EMCA in trigonal tellurium crystals⁵⁸, chiral magnet MnSi⁵⁹ and CoNi microhelices⁶³, so we expect this effect is observable in RhSi. We also point out that although related, CISS is not identical to EMCA, and P_{S_z} is usually different from P_M ⁶² as shown in our calculation. For example, RhSi has $P_{S_z} \approx 0.7\%$ at Fermi energy but much smaller $P_M < 0.25\%$ in the whole bias range. Therefore, the detection of CISS via magneto transport will underestimate the spin polarization in chiral crystals.

In summary, we elucidate and quantify CISS and the associated EMCA response in representative chiral crystals by first-principles quantum transport calculations. The combination of intrinsic homochiral crystal structure and SOC in these crystals leads to simultaneous electron spin and orbital polarization. We demonstrate SOC-enhanced spin polarization in chiral crystals with similar structural and electronic properties, while orbital polarization remains insensitive to SOC. In particular, driven by significant SOC-induced spin splitting at the valence band edge, chiral Te exhibits a substantial spin polarization ratio. The EMCA response in RhSi is investigated and its distinction to the spin polarization is clarified. This work provides essential insights into CISS responses in chiral inorganic crystals, paving the way for applications in spintronics, spin control chemistry and enantiomer recognition.

Calculation details

We performed the density-functional theory (DFT) calculations^{64,65} combined with the Full-Potential Local-Orbital (FPLO) package⁶⁶ to generate highly symmetric atomic-orbital-like Wannier functions and

the corresponding tight-binding (TB) model Hamiltonian of CoSi, RhSi, RhSn, RhBiS, PdAl, PdGa, PtAl, PtGa, and Te. The exchange-correlation potential is described in the generalized gradient approximation (GGA)⁶⁷. The k-point grid was set to $12 \times 12 \times 12$, and the convergence of the total energy convergence was set to 10^{-6} eV. Using the obtained TB Hamiltonian, the quantum transport quantity of the conductance can be calculated based on Landauer-Büttiker formalism in Eq. 1, and the spin and orbital polarized conductance can be calculated by Eq. 2 and 3. The detailed methods of quantum transport calculations are given in the Supplementary Information.

References

1. Siegel, J. S. Homochiral imperative of molecular evolution. *Chirality: The Pharmacol. Biol. Chem. Consequences Mol. Asymmetry* **10**, 24–27 (1998).
2. Liu, Y., Xiao, J., Koo, J. & Yan, B. Chirality-driven topological electronic structure of dna-like materials. *Nat. Mater.* **20**, 638–644 (2021).
3. Yang, Q. *et al.* Monopole-like orbital-momentum locking and the induced orbital transport in topological chiral semimetals. *arXiv preprint arXiv:2307.02668* (2023).
4. Sessi, P. *et al.* Handedness-dependent quasiparticle interference in the two enantiomers of the topological chiral semimetal pdga. *Nat. communications* **11**, 3507 (2020).
5. Chang, G. *et al.* Topological quantum properties of chiral crystals. *Nat. materials* **17**, 978–985 (2018).
6. Yao, M. *et al.* Observation of giant spin-split fermi-arc with maximal chern number in the chiral topological semimetal PtGa. *Nat. Commun.* **11**, 1–7 (2020).
7. Krieger, J. A. *et al.* Parallel spin-momentum locking in a chiral topological semimetal. *arXiv preprint arXiv:2210.08221* (2022).

8. Naaman, R., Paltiel, Y. & Waldeck, D. H. Chiral molecules and the electron spin. *Nat. Rev. Chem.* **3**, 250–260 (2019).
9. Naaman, R., Paltiel, Y. & Waldeck, D. H. Chiral molecules and the spin selectivity effect. *J. Phys. Chem. Lett.* **11**, 3660–3666 (2020).
10. Yang, S.-H., Naaman, R., Paltiel, Y. & Parkin, S. S. Chiral spintronics. *Nat. Rev. Phys.* **3**, 328–343 (2021).
11. Naaman, R. & Waldeck, D. H. Spintronics and chirality: Spin selectivity in electron transport through chiral molecules. *Annu. review physical chemistry* **66**, 263–281 (2015).
12. Zhang, W., Banerjee-Ghosh, K., Tassinari, F. & Naaman, R. Enhanced electrochemical water splitting with chiral molecule-coated fe₃o₄ nanoparticles. *ACS Energy Lett.* **3**, 2308–2313 (2018).
13. Mtangi, W. *et al.* Control of electrons' spin eliminates hydrogen peroxide formation during water splitting. *J. Am. Chem. Soc.* **139**, 2794–2798 (2017).
14. Bian, Z. *et al.* Hybrid chiral mos₂ layers for spin-polarized charge transport and spin-dependent electrocatalytic applications. *Adv. Sci.* **9**, 2201063 (2022).
15. Banerjee-Ghosh, K. *et al.* Separation of enantiomers by their enantiospecific interaction with achiral magnetic substrates. *Science* **360**, 1331–1334 (2018).
16. Stolz, S. *et al.* Asymmetric elimination reaction on chiral metal surfaces. *Adv. Mater.* **34**, 2104481 (2022).
17. Göhler, B. *et al.* Spin selectivity in electron transmission through self-assembled monolayers of double-stranded dna. *Science* **331**, 894–897 (2011).
18. Niño, M. Á. *et al.* Enantiospecific spin polarization of electrons photoemitted through layers of homochiral organic molecules. *Adv. Mater.* **26**, 7474–7479 (2014).

19. Mondal, A. K. *et al.* Spin filtering in supramolecular polymers assembled from achiral monomers mediated by chiral solvents. *J. Am. Chem. Soc.* **143**, 7189–7195 (2021).
20. Ray, K., Ananthavel, S., Waldeck, D. & Naaman, R. Asymmetric scattering of polarized electrons by organized organic films of chiral molecules. *Science* **283**, 814–816 (1999).
21. Ziv, A. *et al.* Afm-based spin-exchange microscopy using chiral molecules. *Adv. Mater.* **31**, 1904206 (2019).
22. Huizi-Rayo, U. *et al.* An ideal spin filter: Long-range, high-spin selectivity in chiral helicoidal 3-dimensional metal organic frameworks. *Nano Lett.* **20**, 8476–8482 (2020).
23. Lu, H. *et al.* Spin-dependent charge transport through 2d chiral hybrid lead-iodide perovskites. *Sci. advances* **5**, eaay0571 (2019).
24. Kim, Y.-H. *et al.* Chiral-induced spin selectivity enables a room-temperature spin light-emitting diode. *Science* **371**, 1129–1133 (2021).
25. Qian, Q. *et al.* Chiral molecular intercalation superlattices. *Nature* **606**, 902–908 (2022).
26. Al-Bustami, H. *et al.* Atomic and molecular layer deposition of chiral thin films showing up to 99% spin selective transport. *Nano Lett.* **22**, 5022–5028 (2022).
27. Adhikari, Y. *et al.* Interplay of structural chirality, electron spin and topological orbital in chiral molecular spin valves. *Nat. Commun.* **14**, 5163, DOI: [10.1038/s41467-023-40884-9](https://doi.org/10.1038/s41467-023-40884-9) (2023). [2209.08117](#).
28. Calavalle, F. *et al.* Gate-tuneable and chirality-dependent charge-to-spin conversion in tellurium nanowires. *Nat. Mater.* **21**, 526–532 (2022).
29. Furukawa, T., Shimokawa, Y., Kobayashi, K. & Itou, T. Observation of current-induced bulk magnetization in elemental tellurium. *Nat. communications* **8**, 954 (2017).

30. Inui, A. *et al.* Chirality-induced spin-polarized state of a chiral crystal CrNb_3S_6 . *Phys. Rev. Lett.* **124**, 166602 (2020).
31. Shiota, K. *et al.* Chirality-induced spin polarization over macroscopic distances in chiral disilicide crystals. *Phys. Rev. Lett.* **127**, 126602 (2021).
32. Zhong, S., Moore, J. E. & Souza, I. Gyrotropic magnetic effect and the magnetic moment on the fermi surface. *Phys. review letters* **116**, 077201 (2016).
33. Xiao, D., Chang, M.-C. & Niu, Q. Berry phase effects on electronic properties. *Rev. modern physics* **82**, 1959 (2010).
34. Ryndyk, D. A. *et al.* Theory of quantum transport at nanoscale. *Springer Ser. Solid-State Sci.* **184**, 9 (2016).
35. Covito, F., Eich, F., Tuovinen, R., Sentef, M. & Rubio, A. Transient charge and energy flow in the wide-band limit. *J. Chem. Theory Comput.* **14**, 2495–2504 (2018).
36. Büttiker, M. Four-terminal phase-coherent conductance. *Phys. Rev. Lett.* **57**, 1761 (1986).
37. Kettner, M. *et al.* Spin filtering in electron transport through chiral oligopeptides. *J. Phys. Chem. C* **119**, 14542–14547 (2015).
38. Wolf, Y., Liu, Y., Xiao, J., Park, N. & Yan, B. Unusual spin polarization in the chirality-induced spin selectivity. *ACS nano* **16**, 18601–18607 (2022).
39. Ōnuki, Y. *et al.* Chiral-structure-driven split fermi surface properties in TaSi_2 , NbSi_2 , and VSi_2 . *J. Phys. Soc. Jpn.* **83**, 061018 (2014).
40. Shishido, H., Sakai, R., Hosaka, Y. & Togawa, Y. Detection of chirality-induced spin polarization over millimeters in polycrystalline bulk samples of chiral disilicides NbSi_2 and TaSi_2 . *Appl. Phys. Lett.* **119** (2021).

41. Yang, Q. *et al.* Topological engineering of Pt-group-metal-based chiral crystals toward high-efficiency hydrogen evolution catalysts. *Adv. Mater.* **32**, 1908518 (2020).
42. Schröter, N. B. *et al.* Observation and control of maximal chern numbers in a chiral topological semimetal. *Science* **369**, 179–183 (2020).
43. Rao, Z. *et al.* Observation of unconventional chiral fermions with long fermi arcs in CoSi. *Nature* **567**, 496 (2019).
44. Zhang, Y., de Juan, F., Grushin, A. G., Felser, C. & Sun, Y. Strong bulk photovoltaic effect in chiral crystals in the visible spectrum. *Phys. Rev. B* **100**, 245206 (2019).
45. Prinz, J., Gröning, O., Brune, H. & Widmer, R. Highly enantioselective adsorption of small prochiral molecules on a chiral intermetallic compound. *Angew. Chem. Int. Ed.* **127**, 3974–3978 (2015).
46. Li, G. *et al.* Observation of asymmetric oxidation catalysis with b20 chiral crystals. *Angew. Chem. Int. Ed.* **62**, e202303296 (2023).
47. Liu, T. *et al.* Linear and nonlinear two-terminal spin-valve effect from chirality-induced spin selectivity. *ACS nano* **14**, 15983–15991 (2020).
48. Rikken, G., Fölling, J. & Wyder, P. Electrical magnetochiral anisotropy. *Phys. Rev. Lett.* **87**, 236602 (2001).
49. Dalum, S. & Hedegård, P. Theory of chiral induced spin selectivity. *Nano Lett.* **19**, 5253–5259 (2019).
50. Yang, X., van der Wal, C. H. & van Wees, B. J. Spin-dependent electron transmission model for chiral molecules in mesoscopic devices. *Phys. Rev. B* **99**, 024418 (2019).
51. Yang, X., van der Wal, C. H. & van Wees, B. J. Detecting chirality in two-terminal electronic nanodevices. *Nano Lett.* **20**, 6148–6154 (2020).

52. Naaman, R. & Waldeck, D. H. Comment on “spin-dependent electron transmission model for chiral molecules in mesoscopic devices”. *Phys. Rev. B* **101**, 026403 (2020).
53. Yang, X., van der Wal, C. H. & van Wees, B. J. Reply to “comment on ‘spin-dependent electron transmission model for chiral molecules in mesoscopic devices’”. *Phys. Rev. B* **101**, 026404 (2020).
54. Xiao, J. & Yan, B. Nonreciprocal nature and magnetochiral charge polarization in chiral molecular devices. *arXiv preprint arXiv:2201.03623* (2022).
55. Krstić, V., Roth, S., Burghard, M., Kern, K. & Rikken, G. Magneto-chiral anisotropy in charge transport through single-walled carbon nanotubes. *The J. chemical physics* **117**, 11315–11319 (2002).
56. Wei, J. *et al.* Magnetic-field asymmetry of nonlinear transport in carbon nanotubes. *Phys. Rev. Lett.* **95**, 256601 (2005).
57. Pop, F., Auban-Senzier, P., Canadell, E., Rikken, G. L. & Avarvari, N. Electrical magnetochiral anisotropy in a bulk chiral molecular conductor. *Nat. Commun.* **5**, 3757 (2014).
58. Rikken, G. & Avarvari, N. Strong electrical magnetochiral anisotropy in tellurium. *Phys. Rev. B* **99**, 245153 (2019).
59. Yokouchi, T. *et al.* Electrical magnetochiral effect induced by chiral spin fluctuations. *Nat. Commun.* **8**, 866 (2017).
60. Aoki, R., Kousaka, Y. & Togawa, Y. Anomalous nonreciprocal electrical transport on chiral magnetic order. *Phys. Rev. Lett.* **122**, 057206 (2019).
61. Qin, F. *et al.* Superconductivity in a chiral nanotube. *Nat. Commun.* **8**, 14465 (2017).
62. Liu, T. & Weiss, P. S. Spin polarization in transport studies of chirality-induced spin selectivity. *ACS Nano* **17**, 19502–19507, DOI: [10.1021/acsnano.3c06133](https://doi.org/10.1021/acsnano.3c06133) (2023).

63. Maurenbrecher, H. *et al.* Chiral anisotropic magnetoresistance of ferromagnetic helices. *Appl. Phys. Lett.* **112**, 242401, DOI: [10.1063/1.5027660](https://pubs.aip.org/aip/apl/article-pdf/doi/10.1063/1.5027660) (2018). https://pubs.aip.org/aip/apl/article-pdf/doi/10.1063/1.5027660/14512894/242401_1_online.pdf.
64. Kresse, G. & Furthmüller, J. Efficiency of ab-initio total energy calculations for metals and semiconductors using a plane-wave basis set. *Comput. Mater. Sci.* **6**, 15–50 (1996).
65. Kresse, G. & Furthmüller, J. Efficient iterative schemes for ab initio total-energy calculations using a plane-wave basis set. *Phys. Rev. B* **54**, 11169 (1996).
66. Koepnik, K. & Eschrig, H. Full-potential nonorthogonal local-orbital minimum-basis band-structure scheme. *Phys. Rev. B* **59**, 1743 (1999).
67. Perdew, J. P., Burke, K. & Ernzerhof, M. Generalized gradient approximation made simple. *Phys. Rev. Lett.* **77**, 3865 (1996).